

Intensity Gradients Technique: Synergy with Velocity Gradients and Polarization Studies

Yue Hu^{1,2}, Ka Ho Yuen², and A. Lazarian²

Department of Physics, University of Wisconsin–Madison, Madison, WI, USA; yue.hu@wisc.edu

Department of Astronomy, University of Wisconsin–Madison, Madison, WI, USA; kyuen2@wisc.edu, alazarian@facstaff.wisc.edu

Received 2019 August 26; revised 2019 October 2; accepted 2019 October 5; published 2019 November 14

Abstract

Magnetic fields are ubiquitous in the interstellar medium but notoriously difficult to study through observation. Making use of the advances in our understanding of MHD turbulence and turbulent reconnection, the velocity gradients technique (VGT) was suggested and successfully applied to study magnetic fields utilizing spectroscopic data. Applying the tools developed for the VGT to intensity statistics, we introduce the intensity gradients technique (IGT) as a complementary tool that can be used synergistically with the VGT. In this paper, we apply the IGT to a diffuse H I region selected from the GALFA-H I survey and compare the intensity gradient (IG) maps with those obtained using velocity gradients, as well as Planck polarization measurements. We demonstrate the possibility of using the IGT and VGT for both studying the magnetic field and identifying shocks in the diffuse interstellar medium. We also explore the ability of the IGT in locating self-gravitating regions and calculating Alfvénic Mach numbers, both alone and in combination with the VGT and polarimetry. We compare the IGT with the histogram of relative orientation, which utilizes IGs to characterize the relative orientation of column density structures and local magnetic fields.

Unified Astronomy Thesaurus concepts: Interstellar medium (847); Interstellar magnetic fields (845); Interstellar dynamics (839)

1. Introduction

The magnetic force is second in importance, after gravity, in the present-day understanding of the universe (Spitzer 1978; Shu 1983; Mouschovias 1991; Krasnopolsky et al. 2012). In an astrophysical setting, magnetic fields are embedded in turbulent conducting plasmas (Larson 1981; Elmegreen & Scalo 2004; Heyer & Brunt 2004; McKee & Ostriker 2007; Chepurnov et al. 2010), making MHD turbulence an accurate description of the state of astrophysical fluids (Beresnyak & Lazarian 2019). To understand the critical astrophysical process, e.g., the process of star formation (Mestel & Spitzer 1956; Galli et al. 2006; Mouschovias et al. 2006; Johns-Krull 2007), it is essential to know both the properties of the turbulent magnetic field and the density of the matter. In particular, it is crucial to know the density enhancement arising from shocks and self-gravitation.

Studies of the magnetic field in cold diffuse gas and molecular clouds commonly employ the starlight polarization and thermal emissions produced by aligned grains (Andersson et al. 2015), as well as molecular line splitting (Zeeman effect) from radio to optical wavelengths (Crutcher et al. 2010; Crutcher 2012). Far-infrared dust polarization measurements cannot only determine the direction of the projected magnetic field $B_{\rm POS}$ but also roughly estimate the magnetic field strength through the Davis–Chandrasekhar–Fermi method (Davis 1951; Chandrasekhar & Fermi 1953).

However, measurements of the magnetic field using farinfrared dust polarization utilize ground-based telescopes, which are affected by the radiative absorption that happens as radiation passes through the Earth's atmosphere. Moreover, the reliability of magnetic field tracing obtained using polarization techniques decreases when grain alignment and radiative torques are weakened by light extinction (Lazarian & Hoang 2007), e.g., in molecular clouds at high optical depths (Andersson et al. 2015). Although line splitting, such as the Zeeman effect, can directly measure the strength of the line-of-sight (LOS) magnetic field B_{LOS} (Crutcher et al. 2010), high sensitivity requirements and long integration times limit the applicability of Zeeman measurements.

The velocity gradients technique (VGT; González-Casanova & Lazarian 2017; Yuen & Lazarian 2017a, 2017b; Lazarian & Yuen 2018a: Lazarian et al. 2018b) was developed as a new method to trace the direction of magnetic fields by using spectroscopic data. The theoretical basis of the technique, discussed in Section 2, is the theory of MHD turbulence and turbulent reconnection. The utility of the VGT has been successfully tested through numerical simulations and comparison with magnetic field morphology predictions of the diffuse interstellar medium and molecular clouds obtained using polarimetry (Hu et al. 2018; Lazarian & Yuen 2018a; Lazarian et al. 2018b; González-Casanova et al. 2019; Hsieh et al. 2019; Hu et al. 2019a, 2019b, 2019c). In addition to tracing magnetic fields, the VGT is also a powerful technique for obtaining the media magnetization level (Lazarian et al. 2018b) and sonic Mach number measurements (Yuen et al. 2018), and it provides a statistical error measure.

The intensity of emissions from both gas and dust provides additional information about the interstellar medium that is different from the information provided by the VGT. It is therefore attractive to investigate the new insight provided by the intensity gradients (IGs). Our goal is to explore the information obtainable through the synergy of the VGT and the intensity gradients technique (IGT) and the IGT on its own.

Soler et al. (2013) proposed the technique termed the histogram of relative orientation (HRO) to characterize the relative orientation of density gradients and local magnetic fields. However, the HRO is implemented in a way and with goals that are radically different from those of the VGT. The HRO is not a technique for tracing magnetic fields but rather one for exploring the statistics of the change of relative orientation of IGs and magnetic fields in response to changes in

column densities. The authors rely on polarization measurements to find magnetic field orientation. The VGT, in contrast, explores the pointwise statistics of the magnetic field and does not require any outside measurements. In addition, some of the VGT ideas and approaches were successfully borrowed and implemented within the HRO as it was evolving (see Soler et al. 2019).

In what follows, we illustrate the theoretical foundation of the IGT in Section 2. In Section 3, we describe the MHD simulation data used in this work. In Section 4, we briefly describe the algorithms used in the implementation of the IGT. In Sections 5 and 6, we show our results obtained using the IGT in numerical simulations and observations, respectively. In Section 8, we discuss the possible application of IGs with the latest development of the VGT. In Section 9, we give our conclusions.

2. Theoretical Motivation and Expectation

2.1. Theory of MHD Turbulence and VGT

The theoretical justification for why velocity gradients trace the magnetic field comes from the theories of MHD turbulence, as well as turbulent reconnection. The theory of MHD turbulence was given a boost by the prophetic study of Goldreich & Sridhar (1995, hereafter GS95). In particular, GS95) predicted that the turbulent eddies were anisotropic and showed that the degree of turbulence anisotropy increases as the scale of turbulent motions decreases. The subsequent study of turbulent reconnection in Lazarian & Vishniac (1999) demonstrated that turbulent reconnection of the magnetic field is an intrinsic part of the MHD turbulent cascade. The eddies perpendicular to the magnetic field direction evolve freely, with magnetic reconnection taking place over just one eddy period. As a result, anisotropic eddies are aligned with the direction of the magnetic field in their direct vicinity, i.e., the local magnetic field direction. The latter is an absolutely crucial element for the VGT, as it testifies that the small velocity fluctuations are well aligned with the local direction of the magnetic field.³ This phenomenon has been confirmed by the numerical studies of Cho & Vishniac (2000) and Maron & Goldreich (2001).

Employing the notion of fast turbulent reconnection, it is obvious that the motions of eddies with size l_{\perp} perpendicular to the local direction of the magnetic field are not constrained by the magnetic field. Thus, they should exhibit hydrodynamic-type statistics, i.e., obey the Kolmogorov law $v_{l,\perp} \sim l_{\perp}^{\frac{1}{3}}$, where $v_{l,\perp}$ is the turbulence's injection velocity perpendicular to the local direction of the magnetic field. By equating the period of Alfvénic wave and turbulent eddy turnover time,

$$\frac{l_{\parallel}}{\nu_{\rm A}} = \frac{l_{\perp}}{\nu_{l,\perp}},\tag{1}$$

where v_A is the Alfvénic velocity, one can obtain the relation between the long and short axes of the eddies (Lazarian & Vishniac 1999):

$$l_{\parallel} \sim l_{\parallel}^{\frac{2}{3}}.\tag{2}$$

In this paper, we will refer to the above expression for $v_{l,\perp}$ and the relation between l_{\parallel} and l_{\perp} as GS95 relations. Note that the

anisotropy relation is not valid in the reference system of the mean magnetic field. The latter, in fact, was a frequent mistake of many researchers who tried to measure the scale-dependent anisotropy from both numerical simulations and observations.

In terms of the VGT, the Kolmogorov scaling means that (1) the gradients of velocity amplitude scale as $v_{l,\perp}/l_{\perp} \sim l_{\perp}^{-2/3}$, i.e., the smallest resolved scales are most important in calculating the gradients; and (2) the measured velocity gradients are perpendicular to the magnetic field at the smallest resolved scales, i.e., they well trace the magnetic field in the turbulent volume. Similar to the case of far-infrared polarimetry, one should turn the direction of gradients by 90° to obtain the magnetic field direction.

2.2. MHD Turbulence and Density Statistics

In MHD turbulence, velocity and magnetic field fluctuations follow the same GS95 relations for the Alfvénic part, which is a dominant part of the MHD cascade (Lithwick & Goldreich 2001; Cho & Lazarian 2002, 2003). The situation is more complicated for the density field. In fact, in Beresnyak et al. (2005), it was shown that for supersonic turbulence, the GS95 relations could be valid for low-value density enhancements, while the relation becomes different for high-value density fluctuations. Further studies, e.g., Kowal et al. (2007), Yuen & Lazarian (2017b), and Xu et al. (2019), show that the high contrast density fluctuations are created by shocks perpendicular to the local direction of the magnetic field. These structures do not obey the GS95 relations. Therefore, the study of density gradients can provide additional information that is not reflected by velocity gradients.

In particular, Kowal et al. (2007) numerically studied subsonic turbulence with the presence of a relatively strong magnetic field. They showed that the spectrum of the density scales is similar to the pressure, i.e., $E \sim k^{-7/3}$. This scaling type is theoretically expected for the polytropic equation of state $p \propto \rho^{\gamma}$, where p is the pressure, ρ is the density, and γ is the polytropic coefficient (Biskamp 2003). As for supersonic turbulence, the density spectrum becomes shallower because shocks accumulate the fluid into the local and highly dense structures. However, Beresnyak et al. (2005) showed that by filtering out high contrast density clumps, the density statistics still exhibit Kolmogorov-type scaling $E \sim k^{-5/3}$ and scale-dependent anisotropy of the GS95 type $l_{\parallel} \sim l_{\parallel}^{2}$.

2.3. Observations of Velocity and Density Fluctuation

Velocity statistics are not directly available from observations. To get insight into velocity statistics, the traditional way is to use velocity centroids (Esquivel & Lazarian 2005). Those were, in fact, first used for the velocity gradient studies (González-Casanova & Lazarian 2017; Yuen & Lazarian 2017a, 2017b). Later, Lazarian & Pogosyan (2000, 2004) developed the theory of statistics of the position–position–velocity (PPV) spectroscopic data cubes, and Kandel et al. (2017b) elaborated on the theory. Based on these theories, it was proposed to use fluctuations of intensity within thin velocity channel maps to trace the velocity gradients (Lazarian & Yuen 2018a).

Similarly, the observations, as a rule, do not provide 3D density distributions but rather column densities. For instance, due to the high degree of mixing of dust and gas, the farinfrared emission of dust reflects the column densities of

The derivations in GS95) for the anisotropy are done using the mean field reference frame. In fact, the GS95 scaling is not valid in this frame of reference.

diffuse interstellar gas. However, the column density information can also be obtained from integrating the spectroscopic data over the LOS velocities. This way of studying is advantageous, as it allows us to separate the contributions of different volumes of emitting/absorbing gas along the LOS. Therefore, in what follows, we focus on obtaining the column density information from the spectroscopic data.

2.4. Density Fluctuations in Thick Channel Maps

Three-dimensional MHD turbulence data, i.e., in position-position-position (PPP) space, is not available in observations, but Lazarian & Pogosyan (2000) explored the possibility of using the statistics of velocity fluctuations in PPV cubes to study turbulence. The subsequent works (Kandel et al. 2016, 2017a) used PPV cubes to detect the anisotropy of velocity distribution that is induced by the magnetic field. However, the information converted from PPP to PPV we see in observations is not trivial, especially about how the density and velocity structures are modified.

Lazarian & Pogosyan (2000) first proposed the concept of velocity caustics to signify the effect of density structure distortion due to turbulent velocities along the LOS. Since the density structure with different velocities is sampled into different velocity channels, the density structure is significantly modified. In Lazarian & Pogosyan (2000), the significance of velocity caustics in PPV cubes is quantified in terms of the density spectral index, with the latter highly dependent on the sonic Mach number M_s (Cho & Lazarian 2002, 2003). When the density power spectrum is steep, i.e., k < -3, the emissivity spectrum of the PPV cube is dominated by the velocity fluctuation. Thus, for such flows, the density fluctuations in thin channels of PPV data are following the turbulent velocity statistics, while the dominance of velocity fluctuation will lead to a shallower emission spectrum if the velocity channels are sufficiently thin. Later studies (Lazarian & Pogosyan 2004, 2006, 2008) revealed that the same classification is also seen in absorption media, and this has been extensively applied to observations (Green 1993; Deshpande et al. 2000; Dickey et al. 2001; Stanimirović & Lazarian 2001; Lazarian & Pogosyan 2004, 2006; Begum et al. 2006; Khalil et al. 2006; Lazarian 2006; Padoan et al. 2006). Lazarian & Pogosyan (2000) gave the criterion for distinguishing the thin and thick channels. For the thick channel,

$$\Delta v^2 > \delta v^2,\tag{3}$$

where v is the velocity component along the LOS, Δv is the velocity channel width, and δv is the velocity dispersion. The criterion to identify the thick channel given in Lazarian & Pogosyan (2000) is a lower limit. The data that contain no channel but accumulate intensity information along the LOS automatically meet the thick channel criterion, for example, the H I column density and dust emission data. Hence, we expect that the IGT proposed in this work (see Section 4) is applicable to those data.

2.5. Properties of Velocities and Densities in MHD Simulations

Density and velocity fields, in general, have different statistics and contain different information. Therefore, velocity and density gradients can behave differently, e.g., in self-gravitating regions and shocks. As shown in Figure 1, high contrast density structures (blue) in an intensity map are perpendicular to the magnetic field,

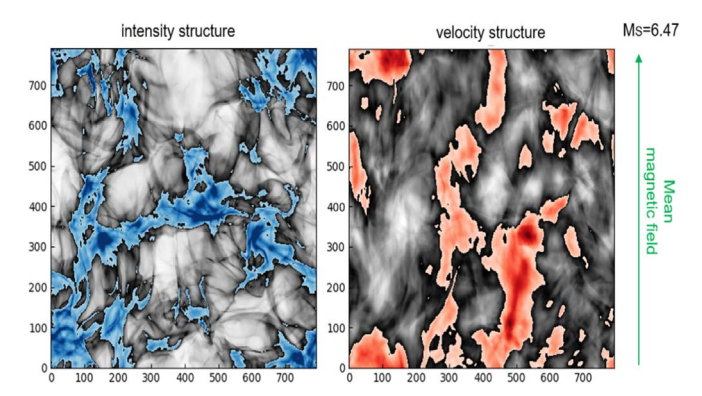


Figure 1. Example of structures in numerical intensity and velocity maps $(M_s = 6.47)$. The colorful isocontours (blue and red) correspond to the region in which its intensity (left)/velocity (right) is larger than the 75th percentile of the full map.

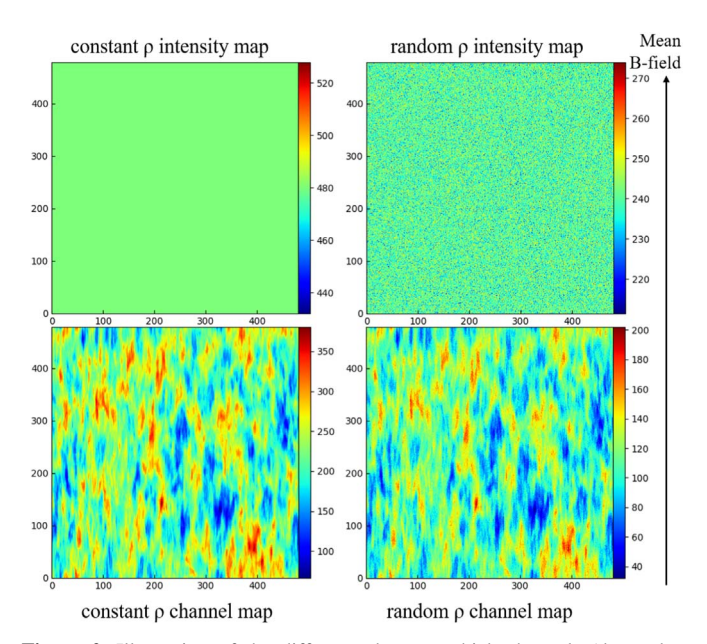


Figure 2. Illustration of the difference between thick channels (denoted as intensity maps; top panel) and thin channels (denoted as channel maps; bottom panel) in the PPV cube. We produce the PPV cubes from the density PPP cube using the (i) constant density field (left column) and (ii) random density field (right column), while keeping the original velocity field unchanged ($M_s = 20$).

but low contrast density structures (gray) are parallel to the magnetic field. These clumpy dense structures that exhibit scale-dependent anisotropy are earlier seen in Beresnyak et al. (2005). They studied moderately magnetized media ($\beta \sim 1$) and found that $E \sim k^{-5/3}$. Later, Xu et al. (2019) explained that perpendicular turbulent mixing of density fluctuations entails elongated low-density structures aligned with the local magnetic field, while high-density filaments compressed by shock are perpendicular to the local magnetic field. However, for velocity structures, they are always parallel to local magnetic fields.

Furthermore, one can study the variation of gradients as the relative contribution of density and velocity changes by varying the thickness of the velocity channels. In Figure 2, we give an illustration of the difference between thick (denoted as intensity map) and thin (denoted as channel map) channels using synthetic observation data. We produce the PPV cubes from the density PPP cube using (i) uniform density distribution and (ii) Gaussian random density distribution while keeping the

original velocity field unchanged ($M_s = 20$). We can see that for both different density distributions, their thin channel maps show similar structures, while their thick channel maps (i.e., intensity maps) are different. Those similar structures in the thin channel are created by velocity caustics; i.e., they are not practical density structures. Therefore, the thin channel map contains more information about the velocity field than the density field, but it is the opposite for intensity maps.

3. MHD Simulation Data

The numerical 3D MHD simulations are generated by the ZEUS-MP/3D code (Hayes et al. 2006), which uses a single-fluid, operator-split, staggered grid MHD Eulerian assumption.

To emulate a part of the interstellar cloud, periodic boundary conditions and solenoidal turbulence injections are applied in our simulations. We employ various Alfvénic Mach numbers $M_{\rm A} = \frac{v_L}{v_{\rm A}}$ and sonic Mach numbers $M_s = \frac{v_L}{v_{\rm S}}$ in our simulations, where v_L is the injection velocity, while $v_{\rm A}$ and v_s are the Alfvénic and sonic velocities, respectively (see Table 1 for details). In the simulations, we also employ various compressibilities $\frac{\beta}{2} = \left(\frac{v_{\rm S}}{v_{\rm A}}\right)^2$ of MHD turbulence. The plasma shows a low compressibility of $\frac{\beta}{2} < 1$ when the magnetic pressure of the plasma is larger than the thermal pressure (i.e., $M_{\rm A} < M_s$, high magnetization level), while the domain $M_{\rm A} > M_s$ corresponds to the pressure-dominated plasma with $\frac{\beta}{s} > 1$.

Furthermore, we refer to the simulations in Table 1 by their model names. For instance, our figures will have a model name indicating which data cube was used to plot the figure. The ranges of M_s and M_A are selected so that they cover different possible scenarios of astrophysical turbulence from very subsonic to supersonic cases. Our simulations in general consider ideal MHD turbulence conditions without the presence for self-gravity, while for simulation M_s 0.2 we take self-gravity into account. The data have been used to set up a 3D, uniform, isothermal turbulent medium (Yuen & Lazarian 2017a, 2017b; Lazarian et al. 2018b; Yuen et al. 2018; Zhang et al. 2019).

4. Methodology

4.1. The IGT

The velocity gradients in thin velocity channels and IGs in thick velocity channels are obtained using an analytical description of PPV (Lazarian & Pogosyan 2000, 2008) cubes. The thin velocity channel map Ch(x, y), in which the velocity contribution in velocity channels dominates over the density contribution, is calculated as

Ch
$$(x, y) = \int_{v_0 - \Delta v/2}^{v_0 + \Delta v/2} \rho(x, y, v) dv,$$
 (4)

where ρ is the gas density, ν is the velocity component along the LOS, $\Delta \nu$ is the velocity channel width satisfied with Equation (4), and ν_0 is the velocity corresponding to the peak position in the PPV velocity profile. The intensity map I(x, y) is produced by the integration of gas density along the velocity axis of the PPV cube. In this case, density fluctuation is dominating I(x, y):

$$I(x, y) = \int \rho(x, y, v) dv.$$
 (5)

We note that in the case of subsonic turbulence, it is advantageous to use velocity centroids to reveal velocity

Table 1
Description of Our MHD Simulations

Set	Model	M_s	$M_{ m A}$	Resolution
	$M_{\rm A}0.2$	7.31	0.22	792 ³
	$M_{\rm A}0.4$	6.10	0.42	792^{3}
	$M_{\rm A}0.6$	6.47	0.61	792^{3}
	$M_{\rm A}0.8$	6.14	0.82	792^{3}
A	$M_{\rm A}1.0$	6.03	1.01	792^{3}
	$M_{\rm A}1.2$	6.08	1.19	792^{3}
	$M_{\rm A}1.4$	6.24	1.38	792^{3}
	$M_{\rm A}1.6$	5.94	1.55	792^{3}
	$M_{\rm A}1.8$	5.80	1.67	792^{3}
	$M_{\rm A} 2.0$	5.55	1.71	792 ³
	$M_{s}0.2$	0.2	0.02	480 ³
В	$M_s 20.0$	20.0	0.2	480^{3}

Note. Here M_s and M_A are the instantaneous values at which each of the snapshots are taken. Each model is simulating a three-dimensional, uniform, and isothermal turbulent medium.

statistics (Esquivel & Lazarian 2005; Kandel et al. 2017b). However, the potential disadvantage of traditional centroids is that the entire spectral line is used, while in some cases, different parts of the spectral line reflect magnetic fields in spatially different regions. This is the case, for instance, for the H I measurements where the galactic rotation curve cannot isolate a particular region of the galaxy. We therefore define the "reduced velocity centroid" map R(x, y), which makes use of part of spectral line only, as

$$R(x, y) = \int_{v_0 - \Delta v/2}^{v_0 + \Delta v/2} \rho(x, y, v) v dv.$$
 (6)

In this work, we denote the gradients calculated from I(x, y) as IGs, while those from Ch(x, y) are velocity channel gradients (VChGs). The study and application of R(x, y), i.e., reduced velocity centroid gradients (RVCGs), is available in Lazarian & Yuen (2018a) and González-Casanova & Lazarian (2019). The gradient angle at each pixel (x_i, y_j) in the plane of the sky (POS) is defined as

$$\nabla_{i,j} f = \tan^{-1} \left[\frac{f(x_i, y_{j+1}) - f(x_i, y_j)}{f(x_{i+1}, y_j) - f(x_i, y_j)} \right], \tag{7}$$

where f(x, y) can be I(x, y), Ch(x, y), or R(x, y). After the pixelized gradient field is established, the subblock-averaging method is applied to predict the direction of magnetic fields through gradients in a statistical region of interest (Yuen & Lazarian 2017a). The use of subblock averaging comes from the fact that the orientation of turbulent eddies with respect to the local magnetic field is a statistical concept. When statistical samples are sufficiently large, the histogram of gradient orientations will show a Gaussian profile (Yuen & Lazarian 2017a). Within a subblock, we obtained the most probable orientation, which is the peak of the Gaussian corresponding to the local direction of the magnetic field within the block.

The correspondence of gradients rotated by 90° and magnetic fields is quantified using the alignment measure (AM): $AM = 2\left(\langle\cos^2\theta\rangle - \frac{1}{2}\right)$, where θ is the relative angle between rotated gradients and orientations of magnetic fields. If the two measures provide identical results, AM = 1, while AM = -1 indicates that the relative angle is 90° .

4.2. Shock Identification Algorithm

The sonic Mach number M_s , which is the ratio of the turbulent injection velocity and the speed of sound, characterizes the compressibility of turbulent flow. When the M_s gets large, i.e., $M_s > 1$, supersonic flows will inevitably form shock waves due to stronger compression. Shocks are a vital process; for instance, MHD simulations by Stone et al. (1998) found that 50% of turbulent energy is dissipated to shocks, and the properties of turbulent gas are significantly modified. As shown in Figure 2, density fluctuation dominates over velocity fluctuation in the thick channel map, i.e., the gas structure in the thick channel is a practical density structure. Therefore, it is potentially possible to identify the shock structure in PPV cubes using the thick channel map. In this work, we propose a new algorithm to identify shock structures using IGs, as well as to study how shocks change the alignment of gradient vectors and the underlying magnetic field.

To start with, we focus on removing the strong J-shocks (Draine 2009). For jump discontinuity, the change of density across shocks is very significant compared to surrounding environments. Therefore, a higher density gradient amplitude is found across the shock front. Hence, we sort out the intensity map according to their amplitudes. Denote the gradient amplitude x, the global mean μ , and the standard deviation σ , and the Z-score of x is defined as (Yuen & Lazarian 2017b)

$$Z(x) = \frac{x - \mu}{\sigma}. (8)$$

A higher positive Z-score stands for regions with gradient amplitudes above the system average. Since areas with higher amplitudes correspond to those with J-shocks, the structure with positive Z-scores is identified as a candidate of shocks.

5. Numerical Simulation Results

5.1. Properties of Gradient Distributions

The VGT was introduced in Lazarian & Yuen (2018b) to obtain a reliable estimation of the magnetization of the media in both H_I data (Lazarian & Yuen 2018b) and molecular clouds (Hu et al. 2019a). As shown in Lazarian et al. (2018b), one could estimate the magnetization through the power-law correlation of the Alfvénic Mach number M_A and the dispersion of the velocity gradient distribution. The distribution of velocity gradient orientations is generally Gaussian. For high magnetization, the distribution is sharply peaked, and the dispersion is small. This corresponds to the excellent alignment of individual gradient vectors and the magnetic field direction. For low-magnetized media, the dispersion increases. As for IGs, their distribution shows similar behaviors as velocity gradients. Figure 3 shows an example of a normalized histogram of gradient orientation without subblock averaging. We see that the distribution of both IG and VChGS orientations is Gaussian, while IGs are more dispersed than VChGs. The uncertainty of the T/B ratio is negligible. This difference can be explained by the presence of shocks in the intensity map. The IGs are gradually changing their direction to be parallel to the magnetic fields when getting close to the shock front. In this case, the distribution of IG orientations gets more dispersion than the one of velocity gradient orientations.

We quantify the gradient dispersions by T/B ratio, where T denotes the maximum value of the fitted histogram of gradient orientations, while B is the minimum value (see Figure 3). The

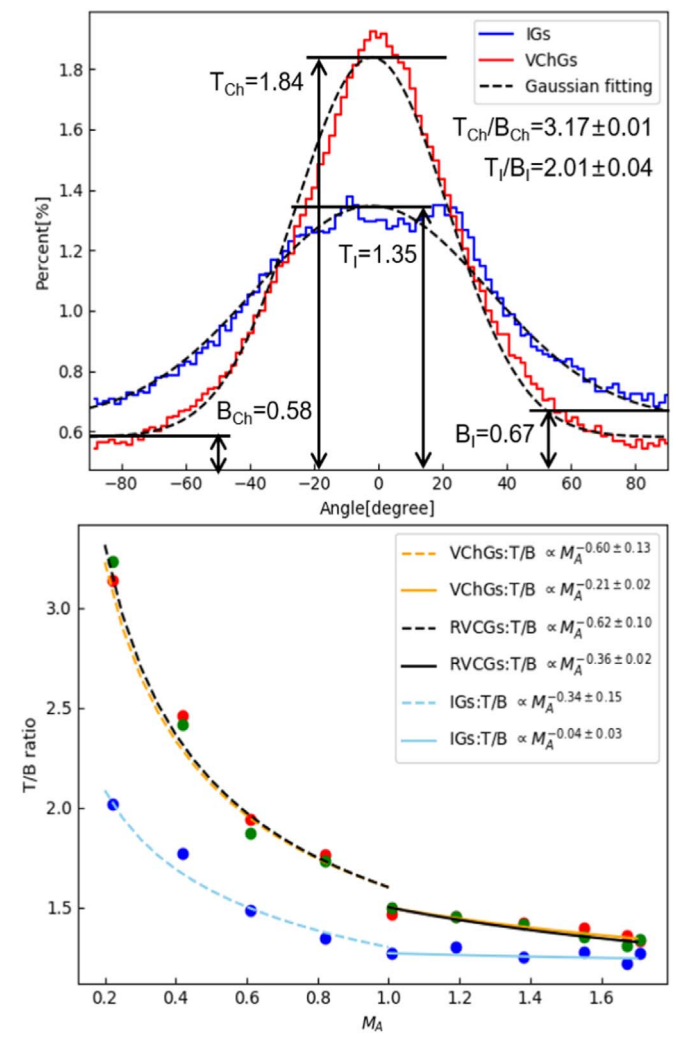


Figure 3. Top: histogram of gradient orientations, where T denotes the maximum value of the fitted histogram, while B is the minimum value. Bottom: correlation between T/B ratio and Alfvén Mach number M_A .

uncertainty is given by the error of Gaussian fitting within a 95% confidential level. Figure 3 shows the correlation of T/Bratio and M_A . We find that, generally, the T/B ratio decreases with the increment of $M_{\rm A}$. There is a well-fit power law of $T/B \propto M_{\rm A}^{-0.60\pm0.13}$ for VChGs, $T/B \propto M_{\rm A}^{-0.21\pm0.02}$ for IGs, and $T/B \propto M_{\rm A}^{-0.62\pm0.10}$ for RVCGs in the case of sub-Alfvénic turbulence $M_{\rm A} < 1$, while $T/B \propto M_{\rm A}^{-0.36 \pm 0.02}$ for VChGs, $T/B \propto M_{\rm A}^{-0.04 \pm 0.03}$ for IGs, and $T/B \propto M_{\rm A}^{-0.36 \pm 0.02}$ for RVCGs when $M_A > 1$. Our results coincide with the results of velocity centroid gradients in Lazarian et al. (2018b). They show $T/B \propto M_{\rm A}^{-0.46\pm0.18}$ for velocity centroid gradients in the case of $M_{\rm A} < 1$. The change in power-law index for $M_{\rm A} > 1$ is expected; as discussed in Lazarian et al. (2018b), the nature of turbulence changes when the injection velocity becomes higher than the Alfvén speed. In this situation, the large-scale motions of eddies are dominated by hydro-type turbulence, and the directions of magnetic fields within flows are significantly randomized. This changes the distribution function of gradient orientations. In addition to the well-fit power law for velocity gradients, including VChGs, RVCGs, and VCGs, IGs also show a corresponding reaction with respect to the variation of magnetization. Therefore, IGs can be used as a complementary

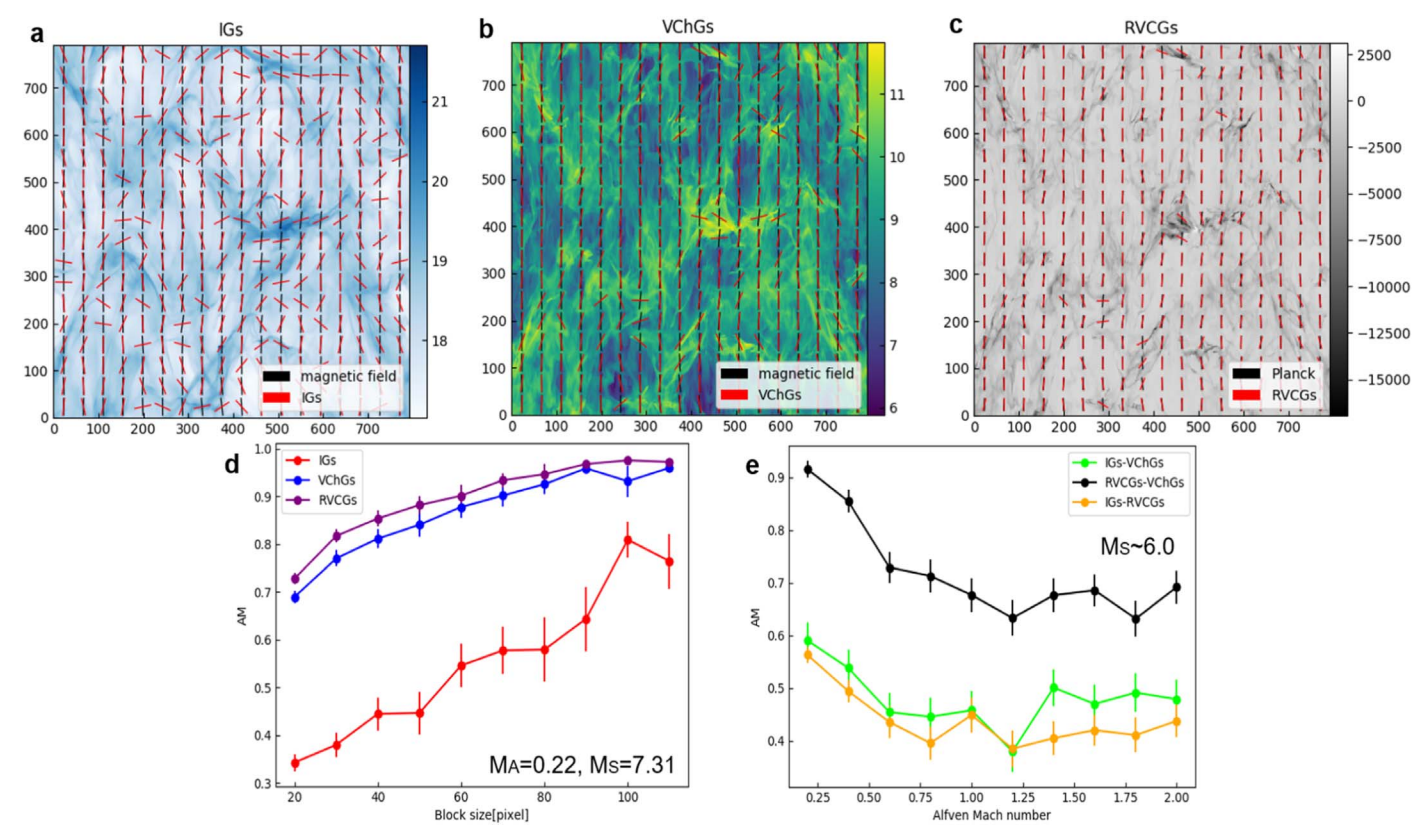


Figure 4. (a)—(c): example of the magnetic fields inferred from IGs, VChGs, and RVCGs, respectively, with subblock averaging applied, using simulation $M_A0.2$. (d): example of the correlation between AM (gradients and polarization) and block size, using simulation $M_A0.2$. (e): variation of the alignment between each gradient type (IGs, VChGs, RVCGs) as a function of M_A .

tool synergetically with the VGT for estimating the magnetization level.

5.2. Tracing Magnetic Field Morphology

From what we discussed in Section 2, it follows that the correlation with magnetic fields is expected not only for velocity gradients but also IGs. In González-Casanova & Lazarian (2017), the relative orientation between IGs and magnetic fields was primarily explored. It was shown that raw IGs (without the subblock-averaging method applied) are not well correlated with the direction of magnetic fields, giving much larger error estimates for the direction of magnetic fields. Hence, we go further by applying the subblock-averaging method⁴ to IGs in order to have a reliable determination of both the direction of the IGs and the statistical significance of this determination. We expect that IGs would be a complementary tool to the VGT in terms of tracing magnetic fields and getting additional information about shocks.

We show an example of IGs and VChGs using the simulation $M_A0.2$. Figure 4 shows 2D vector maps of magnetic fields traced by IGs, VChGs, and RVCGs with a subblock size of 44 pixels. The RVCGs show a better alignment (AM = 0.87 ± 0.02) with the magnetic field than the VChGs (AM = 0.82 ± 0.02) and IGs (AM = 0.47 ± 0.03). The uncertainty is given by the standard error of the mean, that

is, the standard deviation divided by the square root of the sample size.

We further explore the ability of IGs, RVCGs, and VChGs to trace magnetic fields in terms of the subblock size, which corresponds to the measurement scale in observations. Figure 4 shows the AM (between rotated gradients and magnetic fields) as a function of the block size using simulation $M_{\rm A}0.2$. We find that the AMs of IGs, RVCGs, and VChGs are positively proportional to the subblock size. Since a large subblock contains more sample points, the statistical result is more accurate. In addition, RVCGs and VChGs generally give better alignment than IGs, and at a small scale (block size), RVCGs and VChGs still show good alignment (AM $\sim 0.70 \pm 0.01$). As is our theoretical expectation, the velocity fluctuation follows the same GS95 anisotropy relation in all scales, while it is not the case for density fluctuation.

We plot the alignment between different gradients as a function of M_A and M_S in Figure 4, keeping the block size = 44 pixels. We see that for sub-Alfvénic turbulence, the alignment between different gradients is decreasing, while for super-Alfvénic, the AM tends to be stable. The change in trend is similar to the one obtained from gradient distributions, since the nature of turbulence changes when its kinematic property becomes more important than the magnetic filed. In any case, VChGs and RVCGs are well aligned with each other, which demonstrates that VChGs contain the information of the velocity field. Importantly, the correlation, therefore, potentially provides the possibility of measuring M_A using the alignment between different gradients in future studies.

⁴ The subblock-averaging method was initially developed for the VGT (Yuen & Lazarian 2017a). It is not just a smoothing method for suppressing noise in a region but is also used to increase the reliability of important statistical measurements.

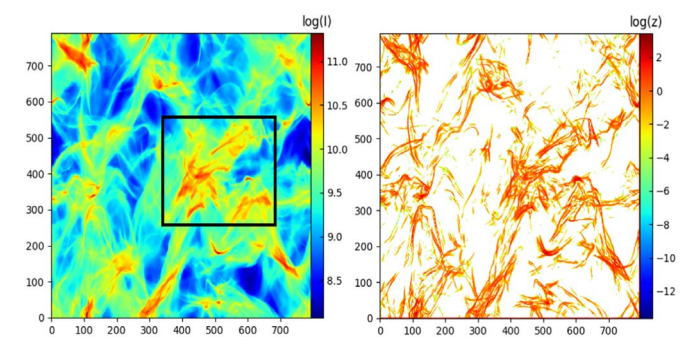


Figure 5. The figure shows how the IG amplitude with a positive Z-score (left) is related to high-density shock structure (right). We use the simulation $M_A 0.4$ here. The black box is indicating a zoom-in region for Figure 7.

In summary, for the subsonic case, the velocity centroid is a better way of representing velocity statistics (Esquivel & Lazarian 2005; Kandel et al. 2017b). Due to the fact that the center of the spectral line is saturated due to absorption effects, it is good to use only the informative part of the line. Therefore, we propose to apply VChGs to trace the magnetic field orientation in supersonic turbulence and RVCGs for subsonic turbulence. As for IGs, they can be used as a complementary tool when velocity information is not available, for example, the H I column density data.

5.3. Identify Shock Structures

High contrast density structures (i.e., shocks) are perpendicular to magnetic fields, but low contrast density structures are parallel to magnetic fields, although this is not the case for velocity structure⁵ (see Section 2.5). In light of this difference, we consider that the higher-contrast shock is one possible obstacle for IGs in terms of tracing magnetic fields.⁶

Figure 5 shows how the shock identification algorithm works on thick channel maps. We sort out the intensity maps according to their Z-scores and wash out the one with a negative Z-score. We see that the IG amplitude with a positive Z-score is well correlated to high-density shock structure. In addition, we sort out IGs according to Z-scores and calculate their AM without applying the subblock-averaging method. Figure 6 shows the plot of the AM as a function of the Z-scores. We see that the alignment is decreasing with higher Z-scores. However, the alignment changes rapidly in the case of a strong magnetic field (low M_A). When the Z-score is more significant than 8, the alignment of $M_A 0.2$ and $M_A 1.0$ is approximately – 0.2, while it is still positive for M_A 2.0. As explained in Xu et al. (2019), high-density filaments compressed by shock are perpendicular to the local magnetic field. Therefore, we expect that the shock can be identified with Z-scores larger than 8 in the case of sub-Alfvénic turbulence. Besides, Soler et al. (2013) concluded that magnetic fields and IGs get parallel when selfgravity is dominating over turbulence. However, our results show that for high M_s turbulence, we can have the change of the relative orientations even without self-gravity.

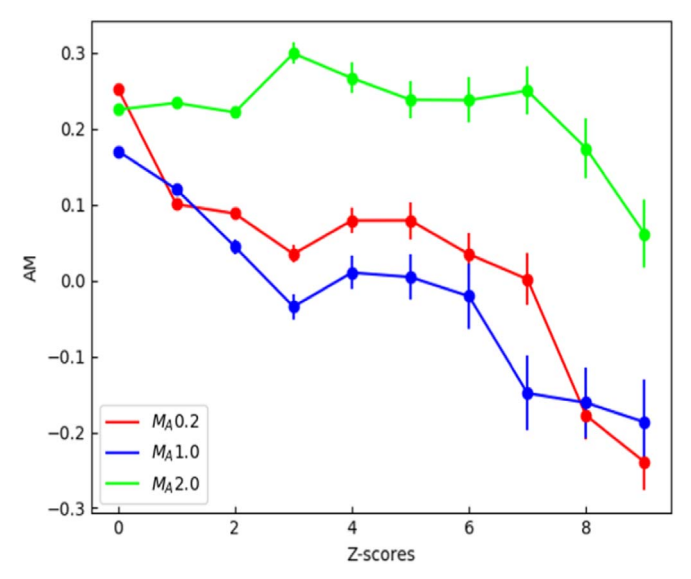


Figure 6. Correlation of AM and Z-scores. Each AM is calculated from raw gradients without subblock averaging and magnetic fields corresponding to the same Z-score, but not the overall AM.

6. Observational Results

To demonstrate the observational applicability of the IGT in tracing the magnetic field and identifying shock structure with the newly developed algorithm, we apply the technique to GALFA-H I spectroscopic data (Peek et al. 2018). The data selected from the GALFA-H I survey correspond to the region stretching from R.A. $\sim 345^{\circ}.35$ to ~ 0.24 . We analyze the H I data with a velocity range from -21 to $21 \, \mathrm{km \, s^{-1}}$. Magnetic field orientation is derived using Planck Collaboration III 2018 PR3 353 GHz polarization data (Planck Collaboration et al. 2018), where the signal-to-noise ratio of dust emission is maximum, as a tracer of the magnetic field. The polarization angle ϕ and POS magnetic field orientation angle θ_B can be derived from the Stokes I, Q, and U parameters using the relation

$$\phi = \frac{1}{2} * \arctan 2(-U, Q)$$

$$\theta_B = \phi + \pi/2.$$
 (9)

The minus sign of U converts the Planck data to IAU convention, where the polarization angle is counted positively from the Galactic north to the east. Before calculating ϕ , one should carefully transform the Stokes U and Q maps from Galactic to equilateral coordinates. As for the calculation of gradients, we implement the subblock-averaging method with a block size equal to 32 pixels (\sim 0°.5) and the moving window method to IGs with a width equal to 2 following Hu et al. (2019a).

Figure 7 shows the B_{POS} morphology inferred from IGs, VChGs, and Planck polarization, as well the shock structure identified by the IGT. Visually, we see that VChGs (AM = 0.68 ± 0.02) align with the magnetic field inferred from Planck polarization better than IGs (AM = 0.45 ± 0.02). However, there is a significant misalignment of IGs and VChGs in the

⁵ Lazarian & Yuen (2018a) showed that gradients rotated by 90° in thin channels get parallel to magnetic fields. It therefore testifies that thin channels are dominated by velocity fluctuations rather than density fluctuations.

Note that thin velocity channels are mixtures of densities and velocities, while the contribution from velocities is dominant over that from densities (Lazarian & Pogosyan 2000). Therefore, although insignificant, the performance of gradients in thin velocity channels is also affected by densities.

⁷ Planck is a project of the European Space Agency (ESA), with instruments provided by two scientific consortia funded by ESA member states (in particular the lead countries France and Italy), with contributions from NASA (USA) and telescope reflectors provided by a collaboration between the ESA and a scientific consortium led and funded by Denmark.

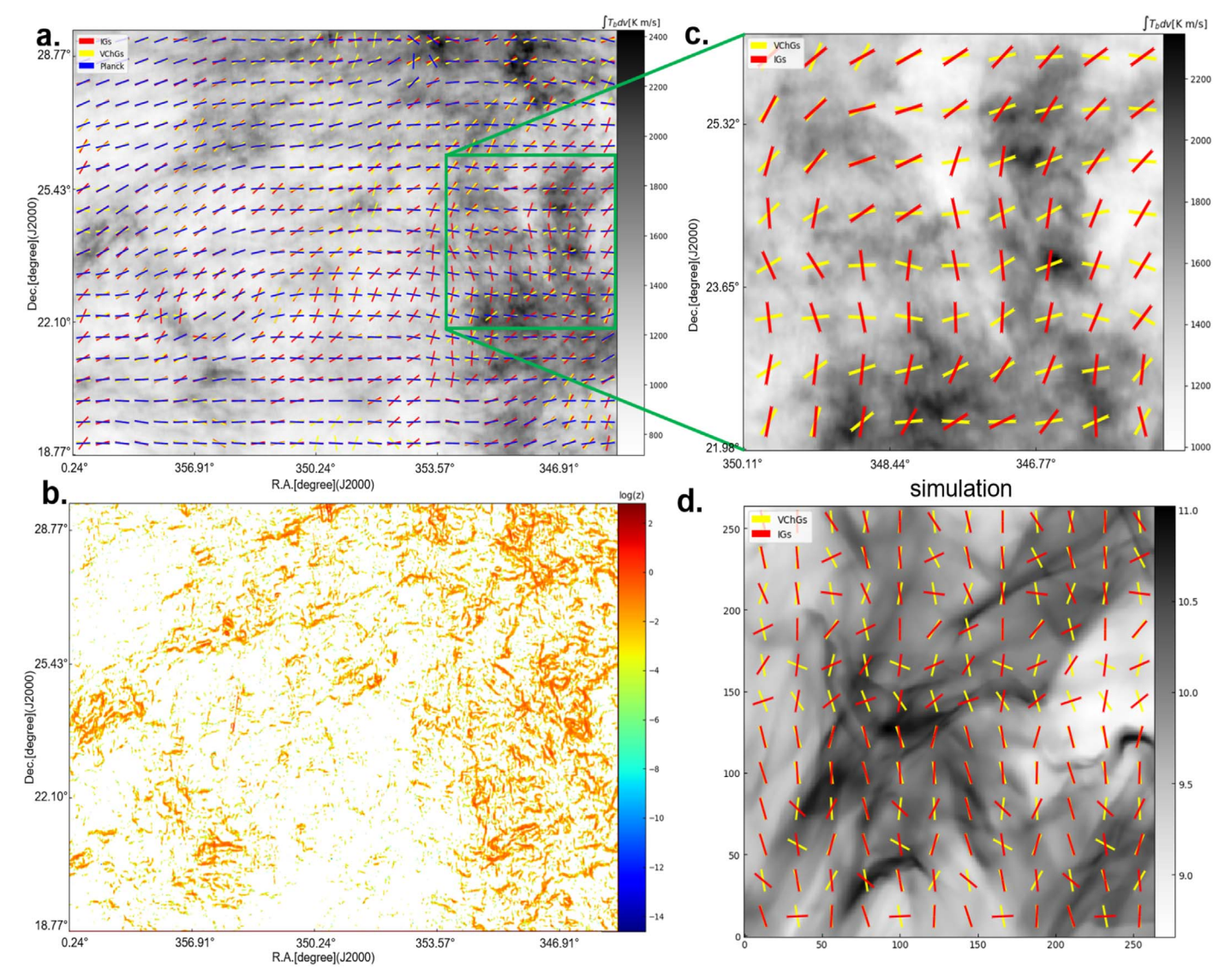


Figure 7. (a): magnetic field morphology predicted by Planck 353 GHz polarization (blue segments), VChGs (yellow segments), and IGs (red segments). The subblock size is selected as 32 pixels (i.e., effective resolution \sim 0°5). (b): shock structure identified using the Z-score algorithm. (c): zoom-in region that shows that IGs and VChGs get to be perpendicular. (d): zoom-in region from our numerical simulation shown in Figure 5.

upper part of Figure 7(a), where we find a lot of shocks. As for the deviation between the gradients and the magnetic fields inferred from Planck polarization, the error from fitting the histogram of gradient orientation within a subblock is one possible contribution. In Figure 8, we plot the variation of the AM with respect to the fitting error in gradients. We bin the fitting error into 10 uniform intervals from zero to $\pi/2$ and take the average value of the AM in each interval. We see that the AM is generally decreasing with the increment of the fitting error. The deviation is, therefore, possibly from the fitting uncertainties.

Also, we plot the histogram of the relative angle between the rotated IGs/VChGs and the magnetic field inferred from Planck polarization in Figure 8 (middle panel). For both IGs and VChGs, the histogram is concentrated on $\sim\!5^\circ$, with AM = 0.68 \pm 0.02 for VChGs and AM = 0.45 \pm 0.02 for IGs. It indicates that VChGs are more reliable and accurate than IGs in terms of magnetic field tracing by comparing with the Planck polarization.

Furthermore, we study the relative orientation between VChGs and IGs. Figure 7 observationally and numerically shows VChGs and IGs in a zoom-in region that is full of shocks in terms of our analysis. We see that IGs and VChGs become perpendicularly aligned. As we illustrated in Figure 1, high contrast density structures compressed by shock show different orientation with respect to velocity structures. Therefore, it confirms LP00's theory that the thick and thin velocity channels contain various information; i.e., the contribution from the velocity field is dominant in narrow velocity channels.

The top panel in Figure 8 shows the variation of raw gradients without subblock averaging with respect to Z-score. Each AM value is calculated from raw gradients and magnetic fields corresponding to the same Z-score but not the overall AM. We see that the AM is negatively proportional to the Z-score, which indicates that the IG tends to be parallel to magnetic fields in front of shocks. This coincides with our numerical simulation results and theoretical considerations. We therefore expect that the structures with Z-scores larger than 10 can be identified as shocks, and we propose to rerotate the raw

Table 2
Comparison of IGT and HRO

Technique	IGT	HRO
Necessity of polarimetry	No	Yes
Trace magnetic field	Yes (limited)	No
Identify gravitational collapse	Yes (with VGT)	No
Trace shocks	Yes (with VGT)	No
Measure $M_{\rm A}$	Yes (limited)	No
Synergy with VGT	Yes	Yes

IGs in front of the shocks by 90° again before implementing the subblock-averaging method.

7. HRO

7.1. Differences and Comparison with HRO

The HRO technique was introduced by Soler et al. (2013), who empirically used a relative orientation angle θ between the density gradient and the magnetic field in each pixel to characterize the direction of column density structures in a histogram form. The IGT is different from the HRO technique, which requires polarimetry data to define the direction of magnetic fields. The IGT is polarization-independent and the way of finding magnetic field direction using the subblock-averaging method. The comparison of the IGT and HRO is summarized in Table 2.

Soler et al. (2019) tried to improve their technique, called the histogram of oriented gradients, which uses gradients in thin velocity channels to systematically compare the gradient contours that might be common HI and 13CO emission. However, Soler et al. (2019) considered the gradients in thin velocity channels as pure IGs. Soler et al. (2019) disregarded the effect of forming intensity fluctuations through the velocity crowding effect (Lazarian & Pogosyan 2000, 2004, 2006, 2008; Begum et al. 2006; Khalil et al. 2006; Lazarian 2006; Padoan et al. 2006; Kandel et al. 2016, 2017a), which is clearly demonstrated in Figure 2. They therefore erroneously assumed that in thin velocity channels, all intensity fluctuations are due to density enhancements. Soler et al. (2019) and Lazarian & Yuen (2018b) used different approaches in the analysis of intensity distributions in thin velocity channels.⁸ The former did not use the procedure of subblock averaging, which is disadvantageous and prevents Soler et al. (2019) from reliably tracing magnetic field direction as it is demonstrated in Lazarian & Yuen (2018b), González-Casanova & Lazarian (2019) and Hu et al. (2019a, 2019b).

To compare the IGT and HRO, we follow the recipe used in Soler et al. (2013), which calculates θ using a combination of the scalar and vector product of vectors

$$\theta = \arctan\left(\frac{|\boldsymbol{B} \times \nabla I|}{\boldsymbol{B} \cdot \nabla I}\right),\tag{10}$$

where B is the magnetic field, while I is the intensity for spectroscopic data. To quantify the progressive change of relative orientation in histogram form (e.g., the HRO curve changes from convex to concave), Soler et al. (2013) defined the histogram shape parameter $\zeta = A_c - A_e$, where A_c is the

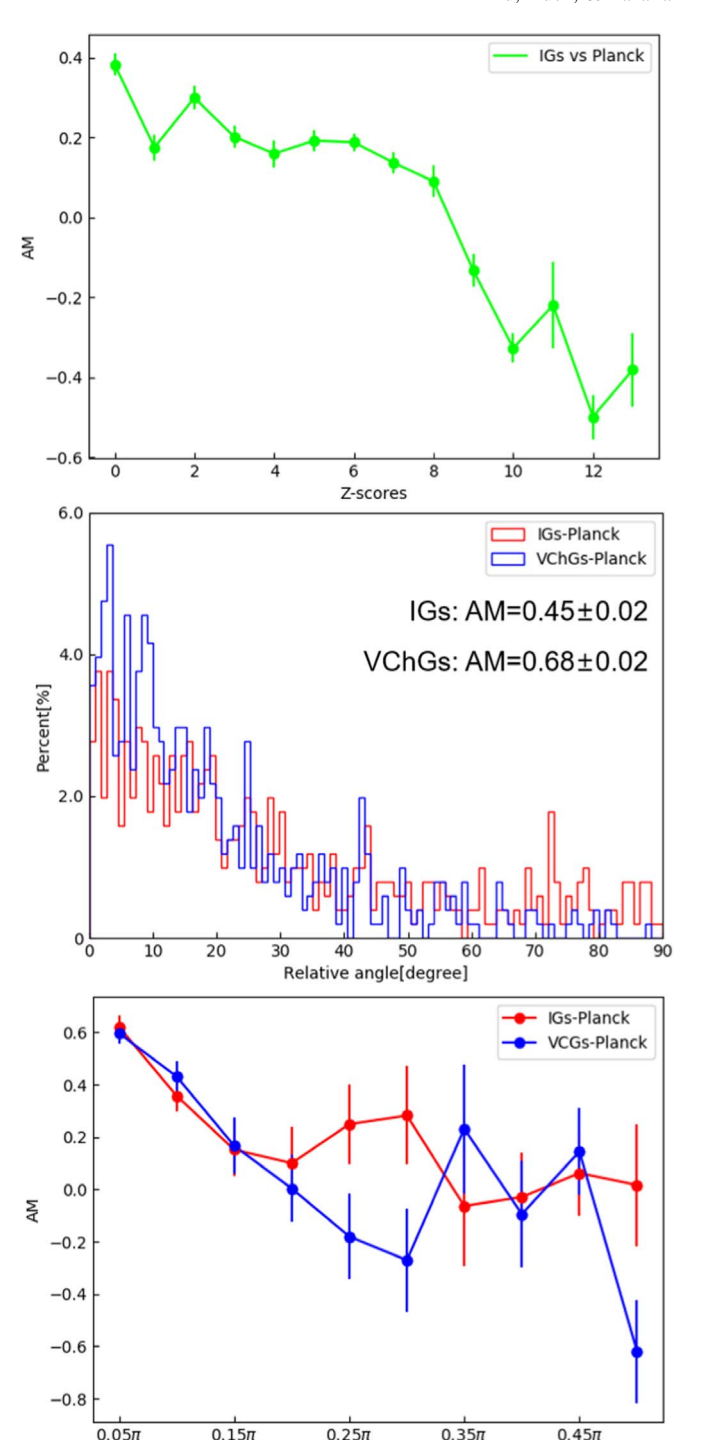


Figure 8. Top panel: plot of AM as a function of Z-scores using raw gradients without subblock averaging. Here AM = 0.0 indicates random distribution, i.e., neither parallel nor perpendicular. Middle panel: histogram of the relative angle between the magnetic field inferred from IGs/VChGs and Planck polarization. Bottom panel: variation of AM with respect to the fitting error in gradients. The error is from fitting the histogram of gradient orientation within a subblock.

Fitting error in gradients

area under the central region of the HRO curve $(-0.25 < \cos\theta < 0.25)$, and A_e is the area in the extremes of the HRO $(-1.0 < \cos\theta < -0.75)$ and $0.75 < \cos\theta < 1.0)$. This parameter characterizes a curve peaking at $\cos\theta \sim 0$ (convex) as $\zeta > 0$, whereas a curve peaking at $\cos\theta \sim \pm 1.0$

The intensity fluctuations in thin velocity channels are the basis of the VChG technique (Lazarian & Yuen 2018b).

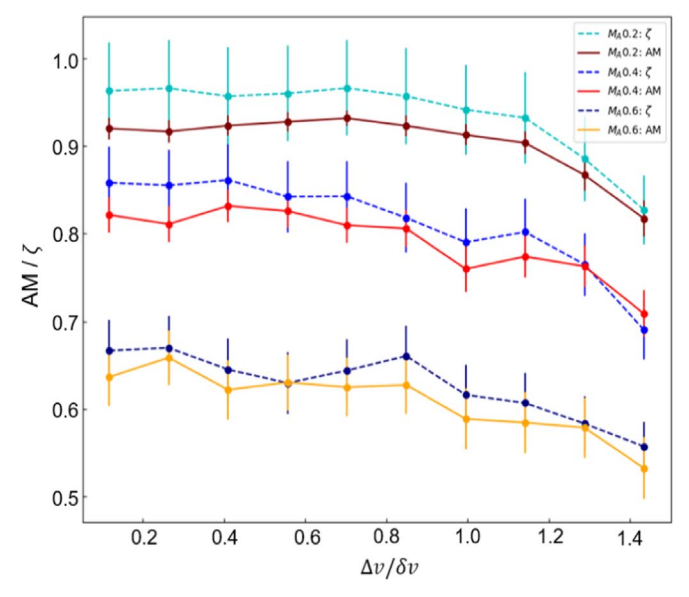


Figure 9. Correlation between $\Delta v/\delta v$ (x-axis) and AM/ ζ (y-axis), where Δv is the velocity channel width, and δv is the velocity dispersion. The dashed line indicates the ζ used in the HRO, while the solid line means the AM used in the gradient technique.

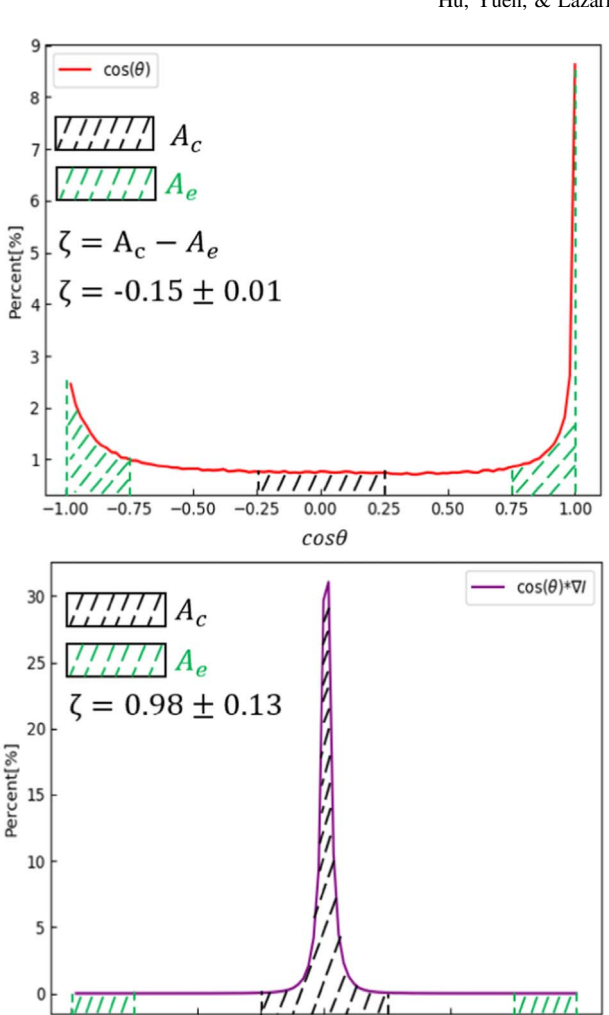
(concave) corresponds to $\zeta < 0$ and a flat distribution corresponds to $\zeta \sim 0$. The uncertainty in the determination of ζ is given by the standard deviation around the calculated area in each region.

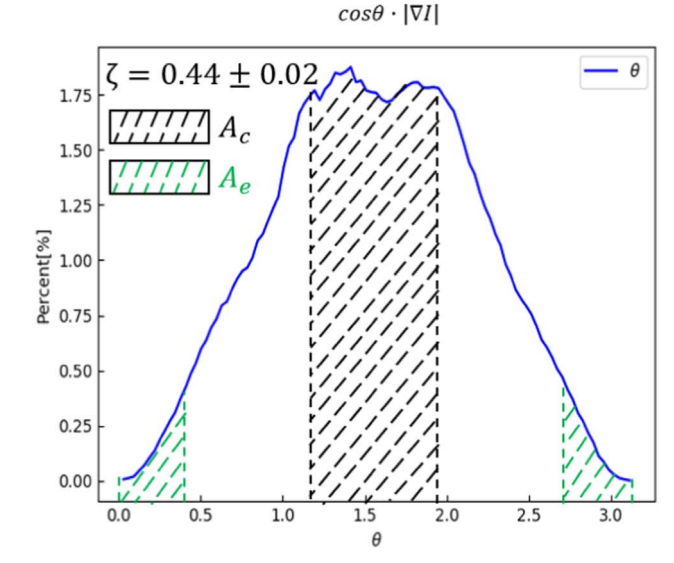
We compare ζ with our AM used in gradient techniques concerning the performance in analyzing the relative orientation between density gradients and magnetic fields. In light of the fact that one can study the relative contribution of density and velocity by varying the thickness of the slice, we also extend the HRO analysis to velocity gradients. Figure 9 shows the correlation of AM/ ζ and the width of the channel. We see that the alignment between gradients and magnetic fields is decreasing for a thicker channel, which is coincident with our theoretical consideration. We find that both the HRO analysis and our AM analysis give similar results, whereas the HRO usually shows a larger value. Although the HRO was initially developed for analyzing density gradients, we show that it is also applicable to velocity gradients in thin channels.

7.2. Modifications to HRO

Soler et al. (2013) used the histogram of $\cos(\theta)$ weighted by $|\nabla I|$ to characterize the relative orientation between density gradients ∇I and B_{POS} . The relative orientation (i) $\zeta > 0$ corresponds to an HRO showing B_{POS} predominantly perpendicular to ∇I , (ii) $\zeta \sim 0$ corresponds to a flat HRO showing no predominant relative orientation between B_{POS} and ∇I , and (iii) $\zeta < 0$ corresponds to an HRO showing B_{POS} predominantly parallel to ∇I .

However, $\cos(\theta) \cdot |\nabla I|$ does not appropriately reveal the information of spatially relative orientation in a histogram format. In Figure 10, we also plot the histograms of $\cos(\theta)$, $\cos(\theta) \cdot |\nabla I|$, and θ using simulation $M_A 0.2$. We see that the histogram of $\cos\theta$ is not a Gaussian, but the histogram of





-0.50

-0.25

0.00

0.25

0.50

0.75

1.00

-0.75

Figure 10. Histograms of $\cos(\theta)$ (top), $\cos(\theta) \cdot |\nabla I|$ (middle), and θ (bottom) plotted in HRO format using simulation $M_A 0.2$. Here $\zeta = A_c - A_e$ is the histogram shape parameter, where A_c is the area under the central region of the HRO curve and A_e is the area in the extremes of the HRO.

 $\cos(\theta) \cdot |\nabla I|$ is shaped to be a Gaussian profile, since the distribution of $\cos(\theta)$ is dominated by the distribution of $|\nabla I|$, which is already a Gaussian itself (Yuen & Lazarian 2017a; Yuen et al. 2018). The distribution of $|\nabla I|$ does not reveal the

⁹ We quote Soler et al. (2013), Section 2.2: "The histogram of values of $\cos \phi$ (ϕ in 2D) weighted by the magnitude of the gradient at each voxel (pixel) is what we call HRO."

orientation of density structures. We clearly see that the histogram of $\cos(\theta)$ is not in Gaussian shape, with $\zeta = -0.15 \pm 0.01$. However, after being weighted by normalized $|\nabla I|$, the histogram becomes Gaussian, with $\zeta = 0.98 \pm 0.13$. Therefore, in terms of studying the relative orientation of B_{POS} and ∇I , the weighted histogram can give different results through the utilization of ζ .

We thus propose removing the weighting term $|\nabla I|$ and using the histogram of θ instead of $\cos\theta$. Since the transformation between θ and $\cos(\theta)$ is not linear, the Gaussian profile of θ is deformed after being transformed into $\cos(\theta)$. In this case, the utility of ζ might cause confusion, as ζ is highly sensitive to the shape of histograms. As shown in Figure 10, ζ illustrates different pictures for the relative orientation of B_{POS} and ∇I . The scientific consideration in Section 2 shows that globally, ∇I tends to be perpendicular to B_{POS} . The histogram of θ thus reveals more accurate physical structures for the relative orientation of B_{POS} and ∇I . An alternative way to accurately quantify the global relative orientation is the utility of the AM, which is implemented in the VGT and not sensitive to the shape of the histograms (see Section 4 for the definition of AM).

7.3. VHRO

In Section 7.2, we modified the HRO by removing the weighting term $|\nabla I|$ and using the histogram of θ . Based on these modifications, we make a synergy of the VGT and HRO techniques, called the velocity HRO (VHRO). The algorithm of the VHRO is following the HRO but using velocity gradients instead of IGs. The ζ is still implemented in the VHRO for simplicity.

In Section 6, we show that IGs may change their orientation to be parallel to magnetic fields at high-density regions in the case of supersonic turbulence. However, in the presence of self-gravity, Yuen & Lazarian (2017b) and Hu et al. (2019a) pointed out that the matter infall induces a change of direction of the intensity/velocity gradients with respect to the magnetic field. In other words, toward regions where star formation is taking place, the intensity/velocity induced by the infall motions parallel to the magnetic field gradually begins to dominate over the intensity/velocity arising from turbulence. As a result, both velocity gradients and IGs are changing their direction by 90°, thus becoming parallel to the magnetic field direction.

Figure 11(a) gives one numerical example of global IGs analyzed by the modified HRO and global velocity gradients in thin channels analyzed by the VHRO in response to the increment of self-gravity. We choose to use the subsonic simulation $M_s0.2$, which has no contribution from shocks. We see that the ζ for both the HRO and VHRO is decreasing as the freefall time increases. It means that the rotated IGs and velocity gradients become perpendicular to the magnetic fields with the increment of self-gravity. However, the change of ζ is more dramatic for IGs. We expect the reason is that the change of density field is an accumulating process, while the velocity field is significantly changed only when the gravitational energy dominates over the kinematic energy of turbulence. This thus provides a way of, first of all, locating regions dominated by self-gravity and second, identifying the stage of

gravitational collapse for molecular clouds using the different behaviors of IGs and velocity gradients.¹¹

In Figure 11(b), we separate the intensity map I(x, y) at freefall time 3.5 Myr into 40 segments. The intensity of the *n*th segment locates at the interval between the $2.5 \cdot (n-1)$ and $2.5 \cdot n$ percentiles of I(x, y). We analysis the relative orientation of intensity/velocity gradients and magnetic fields through the HRO/VHRO in each segment. Here $\zeta = 0.0$ indicates that the relative orientation tends to be neither parallel nor perpendicular, so we claim that when $\zeta \leq -0.1$, the gradients and magnetic fields start changing their relative orientation. In Figure 11(b), we find that the ζ of the HRO is negatively proportional to the intensity in the corresponding segment. It indicates that the IGs are continuously changing their relative orientation from perpendicular to parallel to the magnetic fields. The critical intensity value, above which the change of relative orientation happens, is $I/I_0 \approx 0.4$. However, as for the ζ of the VHRO, we see that there exists a transitional range between $I/I_0 \approx 0.4$ and $I/I_0 \approx 1.0$, at which the value of ζ is oscillating around -0.1. In the case of $I/I_0 \ge 1.0$, the ζ of the VHRO is monotonically decreasing. Therefore, it confirms that velocity gradients change their relative orientation to magnetic fields only when gravitational energy starts dominating the turbulence system.

In Figure 11(c), we plot the gas intensity probability distribution function (PDF), which evolves into a combination of a lognormal (P_N) PDF at low intensities and a power-law (P_L) PDF at high intensities in the case of self-gravitating MHD turbulence (Burkhart & Mocz 2019):

$$P_N(s) = \frac{1}{\sqrt{2\pi\sigma_s^2}} e^{-\frac{(s-s_0)^2}{2\sigma_s^2}}, s \leqslant S_t,$$
 (11)

$$P_L(s) \propto e^{-ks}, \, s > S_t, \tag{12}$$

where $s = \log(I/I_0)$ is the logarithmic intensity and σ_s is the standard deviation of the lognormal, while I_0 and s_0 denote mean intensity and mean logarithmic intensity and S_t is the logarithm of the normalized transitional intensity between lognormal and power-law forms of the intensity PDF. Figure 11(c) shows that when $s \ge S_t \approx 0.17$, the PDF is following a power-low correlation with slope k = 2.15. As a result, when I/I_0 gets larger than $e^{S_t} \approx 1.19$, the gas is expected to be self-gravitating.

In Figure 11(d), we show the intensity contours corresponding to three critical intensity values: (i) $I/I_0 \ge 0.4$ (i.e., IGs start changing the relative orientation; green area enclosed by white contours), (ii) $I/I_0 \ge 1.0$ (i.e., velocity gradients start changing the relative orientation; lime area enclosed by black contours), and (iii) $I/I_0 \ge 1.19$ (i.e., the gas triggers self-gravity; pink contours). We see that all lime areas embed in green areas, while all pink contours are located within the lime area. The close correspondence of the self-gravitating regions and the regions obtained with velocity gradients reveals that velocity gradients analyzed by the VHRO are sensitive in identifying self-gravitating regions. However, this is not the case for density gradients analyzed by the HRO. According to the HRO, only small pieces are not gravitationally collapsing,

 $[\]frac{10}{8}$ For the histogram of θ , and A_c is the area under the central region $\frac{3}{8}\pi < \theta < \frac{5}{8}\pi$, A_e is the area in extreme regions $0 < \theta < \frac{1}{8}\pi$ and $\frac{7}{8}\pi < \theta < \pi$.

¹¹ The change of relative orientation of the velocity gradient and IG is also expected to happen in front of shocks. However, shocks can be distinguished from the self-gravity regions through morphological differences. For example, the curvature of the gradient field for the gravitational collapse is expected to be larger than the curvature of the gradient field for shocks.

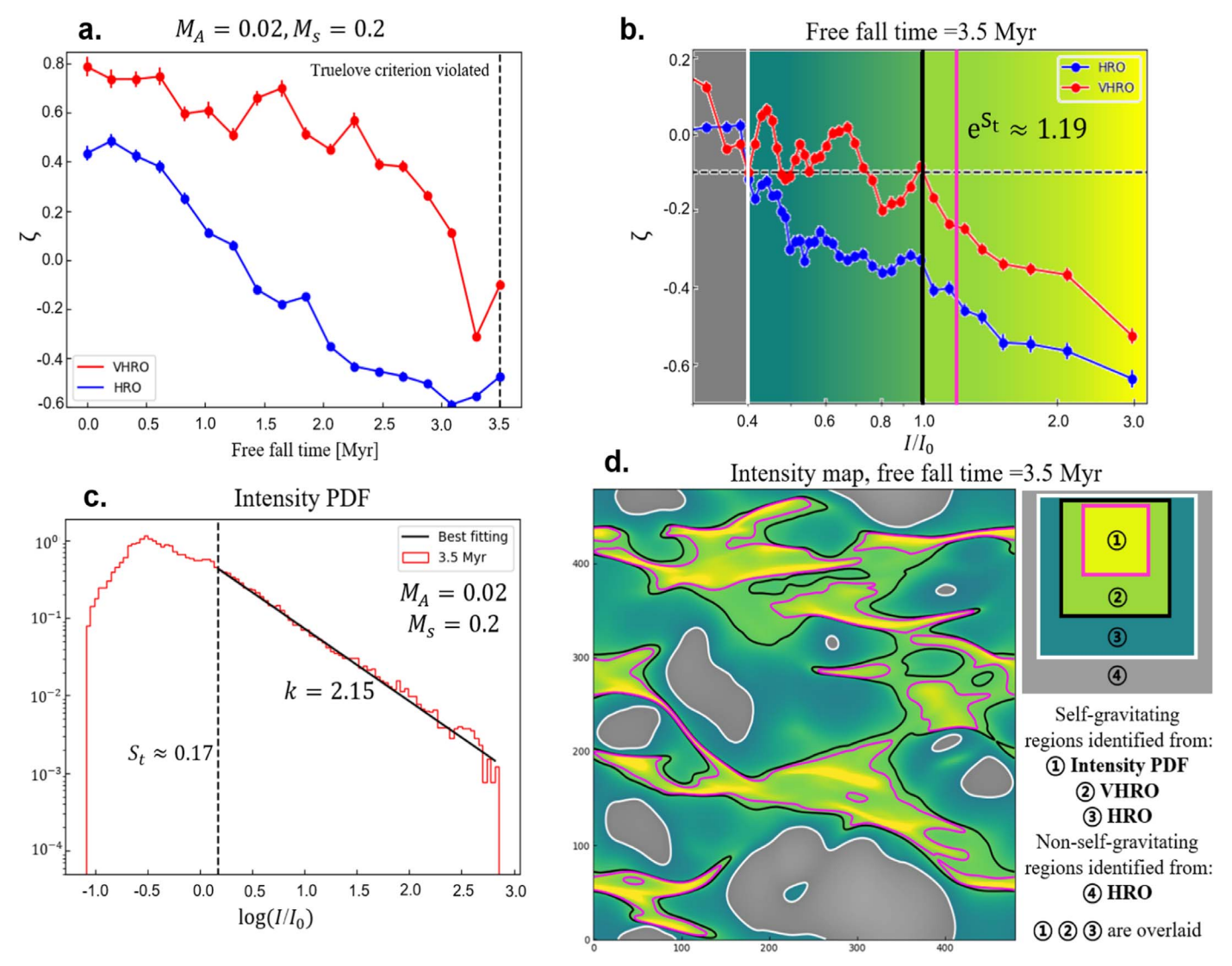


Figure 11. (a): variation of ζ in time after the self-gravity is turned on. The dashed line indicates the time when the Truelove criterion is violated. (b): variation of ζ to different intensity segments I/I_0 , where I_0 is the mean intensity. The dashed line indicates $\zeta = -0.1$. Green represents the starting point of the HRO, while lime represents the starting point of the VHRO. (c): lognormal PDF plus power-law models. The dashed black line outlines all of the density past the transition density S_t , which is self-gravitating. Here k is the slope of the power-law relation. (d): intensity maps of the projection of simulation $M_s0.2$, freefall time 3.5 Myr. Overlaid colors correspond to regions with intensity shown in panel (b).

while in reality, only a small fraction is collapsing. We therefore conclude that the VHRO is more powerful in identifying gravitational collapsing regions than the HRO.

8. Discussion

8.1. Density and Velocity Statistics

In MHD turbulence, density and velocity fluctuations show different statistical behaviors. The velocity fluctuations follow the same GS95 relation for Alfvénic turbulence, while for density fluctuations, the GS95 relation could be valid only by filtering out high contrast density clumps (Beresnyak et al. 2005). The studies of density and velocity fields, therefore, provide different information about MHD turbulence and magnetic fields. For example, Kowal et al. (2007), Yuen & Lazarian (2017b), and Xu et al. (2019) showed that the high contrast density fluctuations are compressed by shocks perpendicular to the local direction of the magnetic field, while velocity structures always remain aligned with their local

magnetic fields. As a result, the density and velocity gradients become perpendicular in front of shocks. Without relying on polarimetry, the study of density and velocity gradients thus provides a possible method for identifying shock structures.

The LP00 theory shows that it is possible to change the relative contribution of density and velocity in PPV cubes. They suggested that density fluctuation dominates in thick velocity channels, while velocity fluctuation dominates in thin velocity channels. This assumption holds not only in the single-phase self-absorption media but also in the two-phase H I media (Lazarian & Pogosyan 2004, 2006, 2008; Chepurnov et al. 2010; Kandel et al. 2017b). Therefore, by varying the thickness of the velocity channels, one can both trace the magnetic field and identify shocks in diffuse regions and molecular clouds.

8.2. Contribution from Thermal Broadening Effect

We propose the IGT as a tool complementary to the VGT. The latter technique has proven successful for studies of both magnetic fields in atomic hydrogen (Yuen & Lazarian 2017a; Hu et al. 2018; Lazarian & Yuen 2018b; Lazarian et al. 2018b; González-Casanova & Lazarian 2019) and molecular clouds (Hu et al. 2019a, 2019b). While gas in molecular clouds presents one-phase media, the existence of two phases of HI induced some researchers to question the validity of the interpretation of the results obtained with the VGT in terms of velocity gradients. In particular, Clark et al. (2019) claimed that the structures observed in thin velocity channel maps arise from actual density structures rather than the velocity caustics as they were interpreted in the papers mentioned earlier (Lazarian & Pogosyan 2004, 2006, 2008; Chepurnov et al. 2010; Kandel et al. 2017b). If this were true, there would be no differences between the studies of IGs within thick slices and velocity gradients using thin slices, i.e., the VChG technique (Lazarian & Yuen 2018b). The results in the present paper contradict this conclusion. First of all, the maps of gradients and the AM obtained with the VChG technique are very different from those obtained with IGs but similar to those obtained with velocity centroid gradients. Moreover, the regions where the directions obtained with IGs and VChGs are different coincide with the shock regions (see Figure 7), and the directions obtained with VChGs and IGs in these regions are close to 90°. The latter are the expectations of the gradient theory based on the modern understanding of MHD turbulence (Beresnyak & Lazarian 2019), and, at the same time, these facts are difficult to explain assuming the structures in the thin and thick velocity channel maps arise from actual enhancements of underlying hydrogen density. Our reply to Clark et al. (2019) is made public in Yuen et al. (2019), and below, we explain why we believe that the measurements of intensities in thin and thick channels deliver velocity and density information, respectively.

Clark et al. (2019) used both GALFA-H I observational data and numerical simulations to address the physical nature of thin velocity channels in PPV space. The study questions the validity and applicability of the statistical theory of PPV space fluctuations formulated in Lazarian & Pogosyan (2000, hereafter LP00) to H I gas. It concludes that (i) the thermal broadening effect washes out the velocity information in thin velocity channels in the case of subsonic turbulence, (ii) the structure in thin velocity channels arises from density fluctuations rather than velocity fluctuations in the case of supersonic turbulence, and (iii) the observed change of spectral index with the evolution of the slice thickness is a consequence of two-phase media effects.

The arguments about the thermal broadening effect raised in Clark et al. (2019) are based on two-phase H I media. However, LP00 already explicitly accounted for thermal broadening and evaluated its effect for both subsonic and supersonic turbulence. They found that the thermal broadening effect gives little contribution to the velocity information in thin velocity channels. Also, the observed change of spectral index is reported by different groups to be the same in both twophase HI media and one-phase media of CO isotopes (Green 1993; Deshpande et al. 2000; Dickey et al. 2001; Stanimirović & Lazarian 2001; LP00, 2006; Begum et al. 2006; Khalil et al. 2006; Lazarian 2006; Padoan et al. 2006). Later, Yuen et al. (2019) argued that the spectral indexes of velocity spectra obtained with LP00 correspond to the expectation of MHD turbulence theory in both observations and numerical simulations. They also illustrate that the computation of the correlation between PPV slices and dust emission in

Clark et al. (2019) is not sensitive in revealing the relative significance of velocity and density fluctuations in velocity channel maps.

It was shown that strong shocks provide density structures that are perpendicular to magnetic fields, while low-density filament structures formed by the shearing fluid are parallel to magnetic fields (Beresnyak et al. 2005; Yuen & Lazarian 2017b; Xu et al. 2019). In the case of low $M_s < 1$ turbulence, therefore, density structures without the presence of shocks are parallel to magnetic fields, in particular for high Galactic latitude regions. As a result, it is not surprising that Clark et al. (2019) got a structural similarity between the Planck 857 GHz dust emission map and H I thin channel maps at high Galactic latitude regions ($b > 60^{\circ}$), since both density and velocity structures are parallel to magnetic fields.

In any case, here we see that IGs can also trace magnetic fields, while VChGs show higher accuracy. Therefore, even in situations where there are significant contributions from density, the validity of VChGs as a technique to trace the magnetic field is not affected.

8.3. Extracting 3D Magnetic Field Structures

Due to the position of the solar system within the Galactic disk, the LOS inevitably crosses more than one molecular cloud. It is therefore impossible to use far-infrared polarimetry to study the local magnetic fields in most molecular clouds. Fortunately, the VGT and IGT show advantages in dealing with multiple-cloud issues. In general, VChGs show higher accuracy than IGs in terms of magnetic field tracing. One possible reason is that the high-density clumps do not show the Goldreich-Sridhar type of anisotropy, although the density structure is always anisotropic at small scales with the presence of strong magnetic fields (Beresnyak et al. 2005). We thus expect that we can improve the performance of IGs in tracing magnetic fields by removing contrast density clumps or low spatial frequencies. In addition, as M_A increases, the magnetic field along the LOS varies rapidly, especially when the turbulence becomes super-Alfvénic. In this case, it is also important to remove the low spatial frequency component.

Hsieh et al. (2019) showed the availability of gradients in tracing magnetic fields using synthetic molecular line maps of the CO isotopologue. After that, Hu et al. (2019b) demonstrated the utility of the VChG technique by using observational data from multiple molecular tracers to construct a 3D magnetic field structure. With the improved IGs, we expect to be able to apply it to 3D magnetic field construction using multiple molecular tracer maps similar to VChGs. One such method would be to stack the IG maps from ¹²CO, ¹³CO, and C¹⁸O to create a three-layer tomography map.

The galactic rotation curve can be used to isolate different clouds, including both diffuse H I and molecular clouds, in the velocity space and allow magnetic fields to be studied separately (González-Casanova & Lazarian 2019). Therefore, it opens new prospects for studying the 3D magnetic field structures in the Milky Way using IGs and VChGs.

9. Conclusion

Based on the theory of MHD turbulence and turbulent reconnection, we show that the IGT, i.e., gradients calculated within thick velocity channel maps, can reveal the magnetic field orientation and magnetization in diffuse media and

identify shock structures. The essence of the technique is to vary the channel thickness to change the relative contribution from density and velocity statistics in PPV space. The gradients of the thick channel maps carry information about the turbulent intensity fluctuation, while the gradients of the thin channel maps contain information about the turbulent velocity fluctuation. We compare the abilities of IGs and the earlier proposed VChG technique, as well as create a synergy with the HRO. We summarize as follows.

- The varying thickness of velocity channels changes the relative contribution from density and velocity statistics. The VChGs calculated within thin velocity channels contain more information about velocity statistics, while the IGs calculated within thick velocity channels contain more information about density statistics.
- 2. We show the following.
 - (a) The dispersions of intensity and velocity gradient distributions are applicable to reveal the magnetization in diffuse media.
 - (b) VChGs and RVCGs are more accurate than IGs in terms of tracing the magnetic field orientation. We propose to trace magnetic field orientation using VChGs for supersonic turbulence and RVCGs for subsonic turbulence.
 - (c) The IGs tend to be parallel to the local magnetic fields when getting close to the dense shock front in the absence of gravity. Therefore, IGs have the advantage of identifying shock structures, while there is no particular universal density at which the change of the relative orientations happens.
- 3. We apply IGs and VChGs to the GALFA-H I data and get statistically similar results. In terms of magnetic field tracing, VChGs show better alignment with the magnetic field inferred from the Planck 353 GHz polarimetry data.
- 4. We claim that the IGT can be used synergetically with the VGT for magnetic field studies when velocity information is not available, for example, the H I column density data.
- 5. We demonstrate the advantages of the synergistic utility of different types of gradients (e.g., IGs, VChGs, RVCGs). We show the possibility of studying magnetic field ecosystems, shocks, and self-gravitational collapse, as well as Alfvénic Mach number.
- 6. We demonstrate significant differences between the HRO and IGT. In particular, the IGT is a technique to be used in conjunction with the VGT, without employing polarimetry, while the HRO critically depends on polarimetry.
- Our work shows how to utilize IGs using the procedures we developed earlier for velocity gradients. We also show the following.
 - (a) Velocity gradients can be used in a way similar to the modified HRO technique for density gradients. The proposed VHRO can be used for identifying the selfgravitating regions.
 - (b) Velocity gradients start to change their relative orientation to magnetic fields when gravitational energy starts dominating the turbulence system.
 - (c) Self-gravitating regions embed in the transition regions obtained with velocity gradients. Velocity gradients are, therefore, sensitive in identifying gravitational collapse.

A.L. acknowledges the support of NSF grants AST 1715754 and 1816234. K.H.Y. acknowledges the support of NSF grant AST 1816234. Y.H. acknowledges the support of NASA TCAN 144AAG1967. This publication utilizes data from the Galactic ALFA H I (GALFA-H I) survey data set obtained with the Arecibo *L*-band Feed Array (ALFA) on the Arecibo 305 m telescope.

Software: ZEUS-MP/3D code (Hayes et al. 2006).

ORCID iDs

Yue Hu https://orcid.org/0000-0002-8455-0805

References

```
Andersson, B.-G., Lazarian, A., & Vaillancourt, J. E. 2015, ARA&A, 53,
Armstrong, J. W., Rickett, B. J., & Spangler, S. R. 1995, ApJ, 443, 209
Begum, A., Chengalur, J. N., & Bhardwaj, S. 2006, MNRAS, 372, L33
Beresnyak, A., & Lazarian, A. 2019, Turbulence in Magnetohydrodynamics
  (Berlin: De Gruyter)
Beresnyak, A., Lazarian, A., & Cho, J. 2005, ApJL, 624, L93
Biskamp, D. (ed.) 2003, Magnetohydrodynamic Turbulence (Cambridge:
  Cambridge Univ. Press), 310
Burkhart, B., & Mocz, P. 2019, ApJ, 879, 129
Chandrasekhar, S., & Fermi, E. 1953, ApJ, 118, 113
Chepurnov, A., & Lazarian, A. 2006, arXiv:astro-ph/0611465
Chepurnov, A., Lazarian, A., Stanimirović, S., Heiles, C., & Peek, J. E. G.
  2010. ApJ. 714, 1398
Cho, J., & Lazarian, A. 2002, PhRvL, 88, 245001
Cho, J., & Lazarian, A. 2003, MNRAS, 345, 325
Cho, J., & Vishniac, E. T. 2000, ApJ, 539, 273
Clark, S. E., Hill, J. C., Peek, J. E. G., Putman, M. E., & Babler, B. L. 2015,
       L, 115, 241302
Clark, S. E., Peek, J. E. G., & Miville-Deschênes, M.-A. 2019, ApJ, 874, 171
Crutcher, R. M. 2012, ARA&A, 50, 29
Crutcher, R. M., Wandelt, B., Heiles, C., Falgarone, E., & Troland, T. H. 2010,
   ApJ, 725, 466
Davis, L. 1951, PhRv, 81, 890
Deshpande, A. A., Dwarakanath, K. S., & Goss, W. M. 2000, ApJ, 543, 227
Dickey, J. M., McClure-Griffiths, N. M., Stanimirović, S., Gaensler, B. M., &
  Green, A. J. 2001, ApJ, 561, 264
Draine, B. T. 2009, in ASP Conf. Ser. 414, Cosmic Dust-Near and Far, ed.
  T. Henning, E. Grün, & J. Steinacker (San Francisco, CA: ASP), 453
Elmegreen, B. G., & Scalo, J. 2004, ARA&A, 42, 211
Esquivel, A., & Lazarian, A. 2005, ApJ, 631, 320
Galli, D., Lizano, S., Shu, F. H., & Allen, A. 2006, ApJ, 647, 374
Goldreich, P., & Sridhar, S. 1995, AJ, 438, 763
González-Casanova, D. F., & Lazarian, A. 2017, ApJ, 835, 41
González-Casanova, D. F., & Lazarian, A. 2019, ApJ, 874, 25
González-Casanova, D. F., Lazarian, A., & Burkhart, B. 2019, MNRAS,
  483, 1287
Green, D. A. 1993, MNRAS, 262, 327
Hayes, J. C., Norman, M. L., Fiedler, R. A., et al. 2006, ApJS, 165, 188
Heyer, M., Gong, H., Ostriker, E., & Brunt, C. 2008, ApJ, 680, 420
Heyer, M. H., & Brunt, C. M. 2004, ApJL, 615, L45
Hsieh, C.-H., Hu, Y., Lai, S.-P., et al. 2019, ApJ, 873, 16
Hu, Y., Yuen, K. H., & Lazarian, A. 2018, MNRAS, 480, 1333
Hu, Y., Yuen, K. H., Lazarian, A., et al. 2019b, ApJ, 884, 137
Hu, Y., Yuen, K. H., & Lazarian, A. 2019c, arXiv:1910.05637
Hu, Y., Yuen, K. H., Lazarian, V., et al. 2019a, NatAs, 3, 776
Johns-Krull, C. M. 2007, ApJ, 664, 975
Kandel, D., Lazarian, A., & Pogosyan, D. 2016, MNRAS, 461, 1227
Kandel, D., Lazarian, A., & Pogosyan, D. 2017a, MNRAS, 470, 3103
Kandel, D., Lazarian, A., Pogosyan, D., et al. 2017b, MNRAS, 464, 3617
Khalil, A., Joncas, G., Nekka, F., Kestener, P., & Arneodo, A. 2006, ApJS,
  165, 512
Kolmogorov, A. 1941, DoSSR, 30, 301
Kowal, G., Lazarian, A., & Beresnyak, A. 2007, ApJ, 658, 423
Krasnopolsky, R., Li, Z.-Y., Shang, H., & Zhao, B. 2012, ApJ, 757, 77
Larson, R. B. 1981, MNRAS, 194, 809
Lazarian, A. 2006, in AIP Conf. Proc. 874, Spectral Line Shapes, ed. E. Oks &
```

M. S. Pindzola (New York: AIP), 301

Lazarian, A. 2009, SSRv, 143, 357

```
Lazarian, A., & Hoang, T. 2007, MNRAS, 378, 910
Lazarian, A., & Pogosyan, D. 2000, ApJ, 537, 720
Lazarian, A., & Pogosyan, D. 2004, ApJ, 616, 943
Lazarian, A., & Pogosyan, D. 2006, ApJ, 652, 1348
Lazarian, A., & Pogosyan, D. 2008, ApJ, 686, 350
Lazarian, A., & Vishniac, E. T. 1999, ApJ, 517, 700
Lazarian, A., & Yuen, K. H. 2018a, ApJ, 853, 96
Lazarian, A., & Yuen, K. H. 2018b, ApJ, 865, 59
Lazarian, A., Yuen, K. H., Lee, H., et al. 2018a, ApJ, 855, 72
Lazarian, A., Yuen, K. H., Ho, K. W., et al. 2018b, ApJ, 865, 46
Lithwick, Y., & Goldreich, P. 2001, BAAS, 33, 90.03
Maron, J., & Goldreich, P. 2001, ApJ, 554, 1175
McKee, C. F., & Ostriker, E. C. 2007, ARA&A, 45, 565
Mestel, L., & Spitzer, L., Jr. 1956, MNRAS, 116, 503
Mouschovias, T. C. 1991, ApJ, 373, 169
Mouschovias, T. C., Tassis, K., & Kunz, M. W. 2006, ApJ, 646, 1043
Padoan, P., Juvela, M., Kritsuk, A., & Norman, M. L. 2006, ApJL, 653, L125
Planck Collaboration, Aghanim, N., Akrami, Y., et al. 2018, arXiv:1807.06207
```

```
Peek, J. E. G., Babler, B. L., Zheng, Y., et al. 2018, ApJS, 234, 2
Shu, F. H. 1983, ApJ, 273, 202
Soler, J. D., Ade, P. A. R., Angilè, F. E., et al. 2017, A&A, 603, A64
Soler, J. D., Beuther, H., Rugel, M., et al. 2019, A&A, 622, A166
Soler, J. D., & Hennebelle, P. 2017, A&A, 607, A2
Soler, J. D., Hennebelle, P., Martin, P. G., et al. 2013, ApJ, 774, 128
Spitzer, L. (ed.) 1978, Physical Processes in the Interstellar Medium (New
  York: Wiley-Interscience), 333
Stanimirović, S., & Lazarian, A. 2001, ApJL, 551, L53
Stone, J. M., Ostriker, E. C., & Gammie, C. F. 1998, ApJL, 508, L99
Vestuto, J. G., Ostriker, E. C., & Stone, J. M. 2003, ApJ, 590, 858
Xu, S., Ji, S., & Lazarian, A. 2019, ApJ, 878, 157
Yuen, K. H., Chen, J., Hu, Y., et al. 2018, ApJ, 865, 54
Yuen, K. H., Hu, Y., Lazarian, A., et al. 2019, arXiv:1904.03173
Yuen, K. H., & Lazarian, A. 2017a, ApJL, 837, L24
Yuen, K. H., & Lazarian, A. 2017b, arXiv:1703.03026
Yuen, K. H., Lazarian, V., & Lazarian, A. 2018, arXiv:1802.00024
```

Zhang, J.-F., Lazarian, A., Ho, K. W., et al. 2019, MNRAS, 486, 4813